High-entropy oxides with a spinel structure as lithium-ion battery anode materials

Fatemeh Ganjali[1], Hadi arabi[1,2,*], Shaban Reza Ghorbani[2], Nasrin Azad[1,3]

[1] Renewable Energies, Magnetism and Nanotechnology Research Laboratory, Faculty of Science, Ferdowsi University of Mashhad, Mashhad

[2] Department of Physics, Faculty of Sciences, Ferdowsi University of Mashhad, Mashhad, Iran

[3] Atikavan Energy part Co., Partlastic group, High Technology Industrial Estate, Mashhad. Iran

ARTICLE INFO	ABSTRACT
	High-entropy oxides (HEOs) are single-phase crystal structures composed of multiple metal elements that provide great potential for energy storage applications due to the synergistic effect of various metal species. They are considered effective anode materials for high-performance lithium-ion batteries (LIBs) because of their structural stability, high electronic conductivity, and ability to create anode materials with novel structures using several elemental compounds. Because the effects of different types of electrochemically active elements on the properties of anode materials are unknown, it is necessary to develop HEOs and investigate their properties. Herein, to explore the electrochemical properties of HEOs by changing the content of cations with various mechanisms for storing lithium, we prepared three samples of HEOs with spinel structure using the solid-state method, one of which is equimolar $(Mg_{0.6}Ni_{0.6}Ti_{0.6}Fe_{0.6}Zn_{0.6})O_4$ and two numbers are near-equimolar $((Mg_{0.6}Ni_{0.6}Ti_{0.3}Fe_{0.9}Zn_{0.6})O_4$ and $(Mg_{0.6}Ni_{0.6}Ti_{0.3}Fe_{0.6}Zn_{0.9})O_4))$. For structural properties determination, X-ray diffraction analysis was used. The results confirmed the formation of three single-phase high-entropy oxides. Electrochemical tests indicated the structural stability of three compounds of high entropy oxides, and the composition of $(Mg_{0.6}Ni_{0.6}Ti_{0.6}Fe_{0.6}Zn_{0.6})O_4$, relative to the others, has better rate capability (163 mAhg^{-1} at 1000 mAg^{-1}) and higher discharge capacity (220 mAhg^{-1} at 200 mAg^{-1}) after 200 cycles.

1. Introduction

Global demand for clean, reliable, and renewable energy sources is increasing because of fundamental limitations to rapidly depleting fossil fuels and severe environmental problems caused by using fossil fuels. Lithium-ion batteries (LIBs) have become the preferred choice for modern energy storage systems, which are significant for industry, transportation, environmental issues, energy storage, and other fields. They are highly intriguing due to their lightweight design, extended cycle life, and high energy density [1–3].

Compared to other rechargeable batteries, such as lead-acid and nickel-cadmium batteries, LIBs exhibit a lighter weight and smaller volume due to their high energy and power density. These features make them promising candidates for hybrid and electric vehicles (EVs). By considering that lithium-ion batteries are one of the most effective ways to power various electric vehicles, there is a need to develop such technology and strive for improved performance of LIBs. One of

High-entropy oxides with a spinel structure as lithium-ion battery anode materials

the research areas to increase the electrochemical performance of LIBs is the improvement of electrode materials, especially the anode materials [4–7].

Commercial graphite anodes with a theoretical capacity of 372 mAhg−1 are currently the most commonly used anode material. This capacity can not meet future requirements. Therefore, transition metal oxides (TMOs) have attracted considerable attention as potential anode materials owing to their high theoretical capacities. However, these materials face problems of structural instability due to electrode cracking and pulverization during lithium insertion/extraction, leading to severe capacity fading and poor speed performance [8,9]. Recently, high-entropy oxides (HEOs) due to their structural stability have received much attention for improving electrode electrochemical performance [10–12].

HEOs are classified as single-phase oxide systems that contain five or more equimolar or near-equimolar cations with concentrations of 5%–35% for each randomly distributed in the corresponding cation network sites. The dependence of the mixing free energy (ΔG_{mix}) on the mixing enthalpy (ΔH_{mix}) and the mixing entropy (ΔS_{mix}) is shown by the thermodynamic Equation (1).

$$\Delta G_{mix} = \Delta H_{mix} - T.\Delta S_{mix} \qquad (1)$$

When ΔG_{mix} be negative the system will be more stable. In a system with a single-phase structure, the ΔG_{mix} will be negative and reach more a stable state. It happens either $\Delta H_{mix} < 0$ or $T.\Delta S_{mix} > \Delta H_{mix}$. If $T\Delta S$ dominates ΔH, give rising to ΔG_{mix} to be negative and an entropy-driven reaction will occur attributed to a single phase high entropy oxide [12–15].

Owing to their unique composition and the synergy caused by the presence of multiple elements, HEOs exhibit several qualitative properties such as high structural stability and high ionic conductivity. Therefore, the compositional flexibility of this category of materials leads to the good capability of HEOs for adjusting their functional characteristics [12,16].

Research has shown that among the different structures, HEOs with a spinel structure are the most interesting. This structure has two Wyckoff sites, octahedral and tetrahedral, that offer an expanded range of divalent and trivalent cations and provide three-dimensional (3D) Li$^+$ transport paths. These features cause high-entropy spinel oxides (HESOs) to enhance reversible capacity. Nevertheless, this variety of multivalent metal cations also complicates the lithium storage mechanism [17,18].

The combination of different lithium storage mechanisms (conversion mechanisms and alloying mechanisms) in a single compound is one of the ways to improve the electrochemical performance of anodes [19], which is made possible by using HEOs with the advantage of simple synthesis methods without expensive additives [20]. Despite the unpredictability of the properties of HEOs due to the uncertainty of the basic mechanisms governing their properties, the extraordinary properties observed in these compounds are a strong motivation for research on HEOs [21–24].

In the present study, the effect of changing the molar concentration of the elements is investigated with different storage mechanisms of lithium, (Ti) with intercalation mechanism, zinc (Zn) with alloying mechanism, and iron (Fe) with conversion mechanism. Three high-entropy oxides, one equimolar composition $(Mg_{0.6}Ni_{0.6}Ti_{0.6}Fe_{0.6}Zn_{0.6})O_4$ and two near-equimolar composition $((Mg_{0.6}Ni_{0.6}Ti_{0.3}Fe_{0.9}Zn_{0.6})O_4,$ $(Mg_{0.6}Ni_{0.6}Ti_{0.3}Fe_{0.6}Zn_{0.9})O_4))$ are synthesized and their structural and electrochemical properties are studied.

2. Method

2.1. Chemical reagents

Iron (III) oxide (Fe_2O_3, 96.5%), magnesium oxide (MgO, 98.0%), nickel (II) oxide (NiO, 99.5%), zinc oxide (ZnO, 99%), titanium oxide (TiO_2, 99.5%) were used as the metal precursors and Ethyl alcohol ($\geq$ 99.7%).

2.2. Preparation

The HESO samples were synthesized using the solid-state method. Stoichiometric amounts of metal oxides were weighed to prepare equimolar composition (HESO1: $(Mg_{0.6}Ni_{0.6}Ti_{0.6}Fe_{0.6}Zn_{0.6})O_4$) and near-equimolar compositions (HESO2: $(Mg_{0.6}Ni_{0.6}Ti_{0.3}Fe_{0.9}Zn_{0.6})O_4$, HESO3: $(Mg_{0.6}Ni_{0.6}Ti_{0.3}Fe_{0.6}Zn_{0.9})O_4$), and then added into the ball mill jar. After that, some grinding balls and Ethyl alcohol are added to the jar and milled for 8 h at 550 rpm and then dried at 80 °C for 4 h. The pre-mixed powders were sintered in a muffle-type furnace. The samples of HESO1 and HESO2 were heated at 950 °C for 8 h and HESO3 at 1100°C and then naturally cooled to room temperature.

Table 1: Test Matrix and Test Conditions

Sample	Composition	Milling Speed (rpm), Milling Time (h)	Drying Temperature (°C) after Milling	Sintering Temperature (°C), Sintering Time (h)
HESO1	$(Mg_{0.6}Ni_{0.6}Ti_{0.6}Fe_{0.6}Zn_{0.6})O_4$	550, 8	80	950, 8
HESO2	$(Mg_{0.6}Ni_{0.6}Ti_{0.3}Fe_{0.9}Zn_{0.6})O_4$	550, 8	80	950, 8
HESO3	$(Mg_{0.6}Ni_{0.6}Ti_{0.3}Fe_{0.6}Zn_{0.9})O_4$	550, 8	80	1100, 8

The experimental variables are shown in Table 1.

2.3. Characterization

The crystalline structure of the HESO samples was examined using an X-ray diffractometer (XRD, Rigaku) with a Cu Ka radiation source. The diffraction angle was scanned from 10 to 90º. Thermogravimetric analysis (TGA) and differential thermal analysis (DTA) were performed at a rate of 5 °C/min in air, ranging from 25 ºC to 1250 ºC.

2.4. Electrochemical property measurements

The three HESO's CR2032 coin cells underwent electrochemical performance testing. The cells were assembled in a glove box filled with Ar, and the levels of H_2O and O_2 were kept below 0.01 ppm. The Active material (80 wt%) were uniformly homogeneously mixed with carbon black (10 wt%) and polyvinylidene fluoride (PVDF) (10 wt%) in an appropriate ratio and then dissolved in N-methyl pyrrolidone (NMP). After stirring the resulting slurry, it coated on a 9 µm thick piece of Cu foil with a blade gap of 100 µm. Then the anode electrode was dried in the vacuum coating drying chamber for 1 h at 90 ºC. Finally, the anode electrode was kept in a vacuum oven at 120 ºC for 12 h.

Lithium foil and 1 M $LiPF_6$ were used as the reference electrode and electrolyte respectively. Galvanostatic measurements of the charge and discharge process were evaluated using the Neware battery tester model BTS4008-5mV-5mA/10mA at various voltages ranging from 0.01 to 3.0 V at 25 ºC. Electrochemical impedance spectroscopy (EIS) measurements were conducted in the frequency range of 100 kHz to 10 MHz at 25 ºC.

3. Results and discussion

3.1. Structure characterization of HESO materials

To study the variation of thermal behavior for defining the appropriate calculation temperature of the HESO1 sample before the calcination process, differential thermal analysis (DTA) and thermogravimetric analysis (TGA) were performed. As shown in Figure 1, the DTA thermogram shows three endothermic peaks at 129.7 °C, 696 °C, and 870.1 °C.
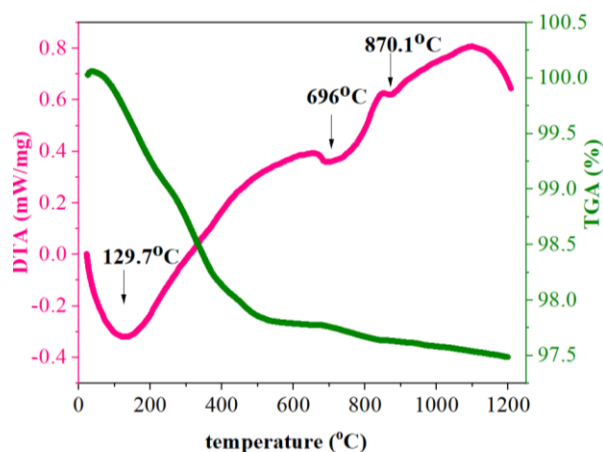

Figure 1: DTA and TGA curve of HESO1 sample after milling.

The first peak of DTA is associated with a weight loss of about 2.2% in the TGA curve, related to the removal and evaporation of species physically attached to the oxide surface [25]. The second peak is associated with a weight loss of about 0.02%, indicating the start of solid solution formation. The third peak also demonstrates the dissolution of the residual oxides [26]. The absence of significant weight loss up to 1200 °C indicates that the reactions occurred before the temperature of 950 °C, and the system is stable after that, so we chose 950 °C as the calcination temperature.

High-entropy oxides with a spinel structure as lithium-ion battery anode materials

Figure 2 shows the X-ray diffraction patterns of HESO samples. For each sample, the presence of the main diffraction peaks at 30.08, 35.43, 43.05, 56.94, and 62.52 corresponding to (220), (311), (400), (511), and (440) planes, respectively, confirming the formation of cubic spinel structure with Fd-3m space group (JCPDS#00-017-0465). As shown in Figure 2, there is no excess peak spectrum, indicating the high purity of the single-phase structured materials.

It should be mentioned that for the HESO3 sample, the sintering temperature of 950 ºC was not enough to create the single phase. At this temperature, impurity peaks were observed in the X-ray diffraction pattern implying 950 ºC is not sufficient to suppress the mixing enthalpy (ΔH_{mix}). To form a single phase, a higher temperature compensation was needed (equation (1)). Therefore, by increasing the temperature up to 1100 ºC, the pure spinel phase of this sample was obtained [24,27].

By comparing the XRD patterns of the three samples, one can deduce that the diffraction peaks in HESO1 are located at a lower angle, indicating the larger lattice parameters of HESO1. Research has shown that larger lattice parameters are generally considered beneficial for Li mobility because more open space facilitates atomic motion [23,28,29].

3.2. Electrochemical performance of the HESOs anodes

The charge-discharge profiles and the differential capacity curves (i.e., dQ/dV plots) of the HESO samples for the first three cycles are shown in Figure 3.

Figures 3a, b, and c show the charge/discharge curves of the HESOs at a current density of 20 mAg^{-1}. The first discharging curves of HESO1 and HESO3 show a sloping platform without a distinct voltage plateau. In the case of HESO2, a short voltage plateau below 0.6 V followed by a slope is observed. These observations show a continuous reaction process associated with the multiple-step reaction process of HEOs [10].

Figures 3d, e, and f show the (dQ/dV) profiles of the three electrodes. For the HESO1 in the first cycle, during the discharge process, there are two peaks at 0.25 and 0.64 V, which can be attributed to the reduction reactions of oxides to the corresponding metal component, the destruction of crystal structure, and the formation of a solid electrolyte phase (SEI). In the charging process, there are two peaks at 0.74 and 1.5 V, which probably be assigned to the oxidation reaction of metallic elements.
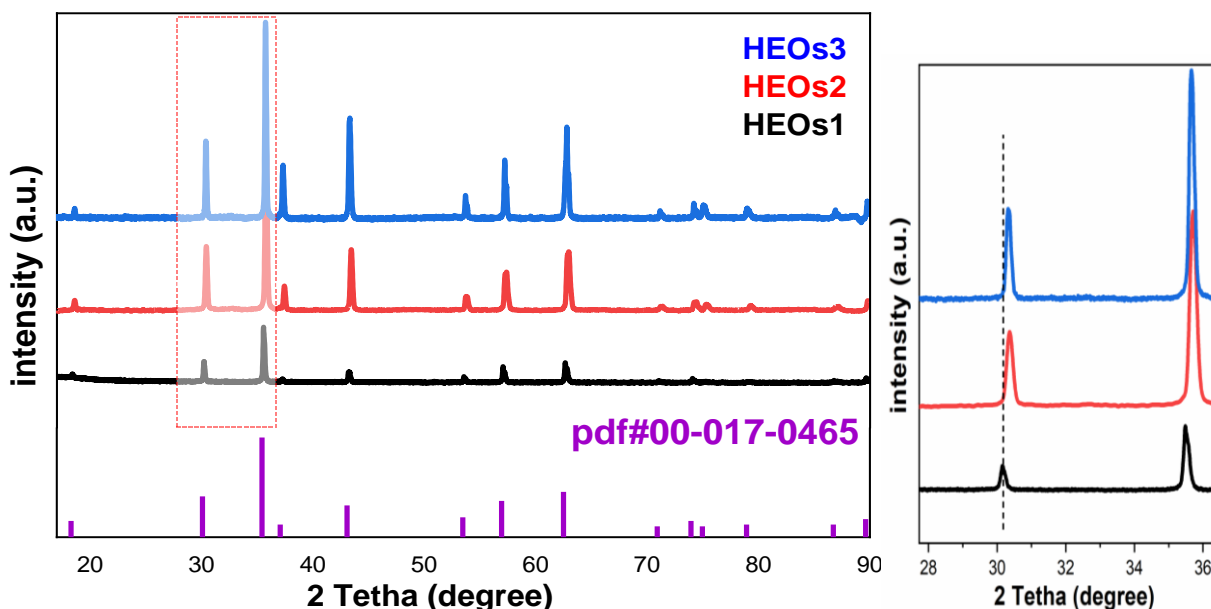

Figure 2: XRD patterns of HESOs.

In the second and third cycles, the cathode peaks are shifted to higher potentials accompanied by a decrease in the intensity of oxidation peaks, which can be caused by the polarization of the anode material and decreasing in crystal size during the first lithiation process [15,30]. The curves overlap to a large extent and also have similar shapes, indicating that the redox reactions are reversible. The absence of a sharp cathode peak indicates the tendency of the formed SEI layer to be stable [31].

The cycle performance of HESOs at 200 mAg^{-1} is depicted in Figure 4a. During the first cycle, the capacity of each of the three anodes drops rapidly before gradually increasing. This phenomenon, which is called U-like increase, is usually found in transition metal oxide materials. The initial decrease in capacity is attributed to complex reactions and irreversible structural transformation including electrolyte decomposition and SEI formation [10,32].
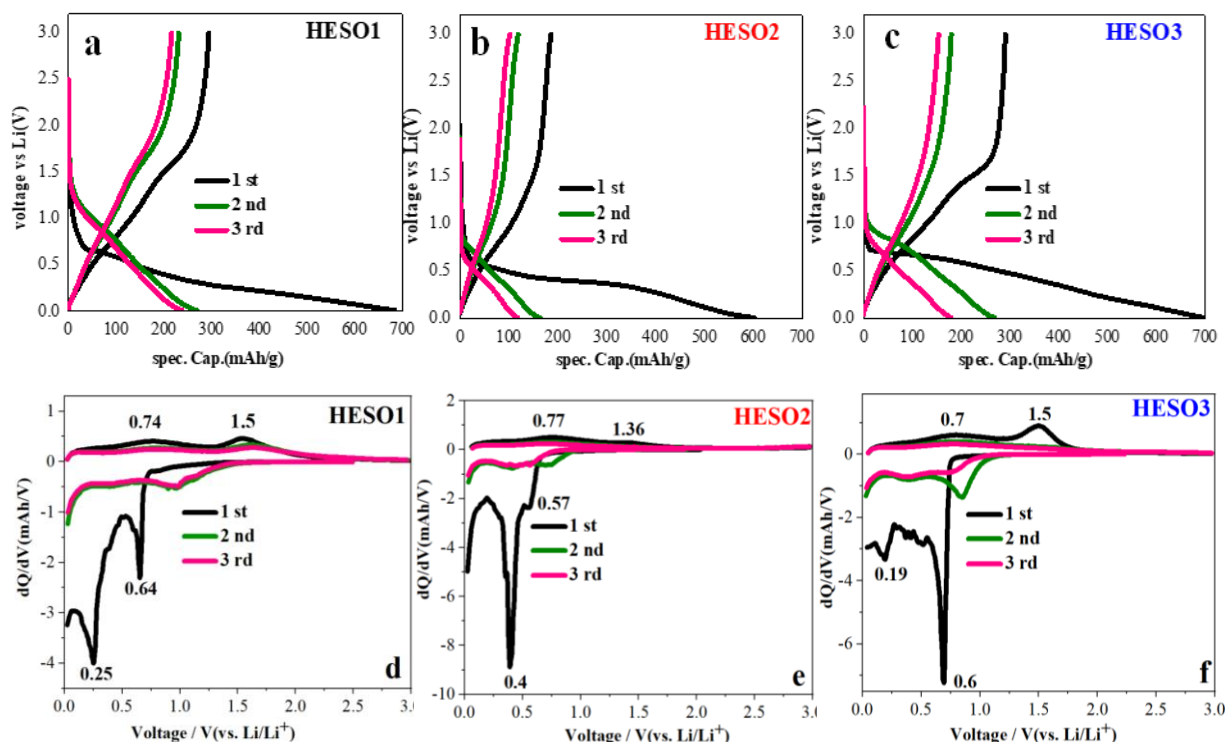

Figure 3: Charge/discharge profiles and dq/dv plots of the HESOs.

As shown in Figures 3e and 3f, in the first cycle of dq/dv plots, the cathodic peaks of HESO2 and HESO3 are located at (0.4 and 0.57 V) and (0.19 and 0.6), respectively. These peaks correspond to the reduction reactions of the oxides, the destruction of crystal structure, and the formation of the solid electrolyte phase (SEI). Anodic peaks corresponding to the oxidation reaction of metallic elements are at (0.77 and 1.36) for HESO2 and at (0.7 and 1.5 V) for the HESO3 sample. For these samples, we can also see a shift of the cathode peaks to higher voltages and a decrease in the intensity of the peaks. In addition, there is no good overlap in the curves of the second and third cycles, demonstrating that the evolution and growth of the SEI layer continue for the HESO2 and HESO3 samples.

All three electrodes show a gradual increase in capacity, which occurs due to the activation process [33]. The activation of large particles through the gradual penetration of the electrolyte into the active materials as well as the rearrangement of the structure of HESOs improve the capacity [23,34,35]. During the 200 cycles at 200 mAg^{-1}, the electrodes show good cycling stability due to entropy stabilization. After 200 cycles, HESO1, HESO2, and HESO3 can achieve the specific capacities of 220, 100, and 140 mAhg^{-1}, respectively, which HESO1 sample presented a higher capacity.

The rate capability of various electrodes measured at various current densities of 50, 100,
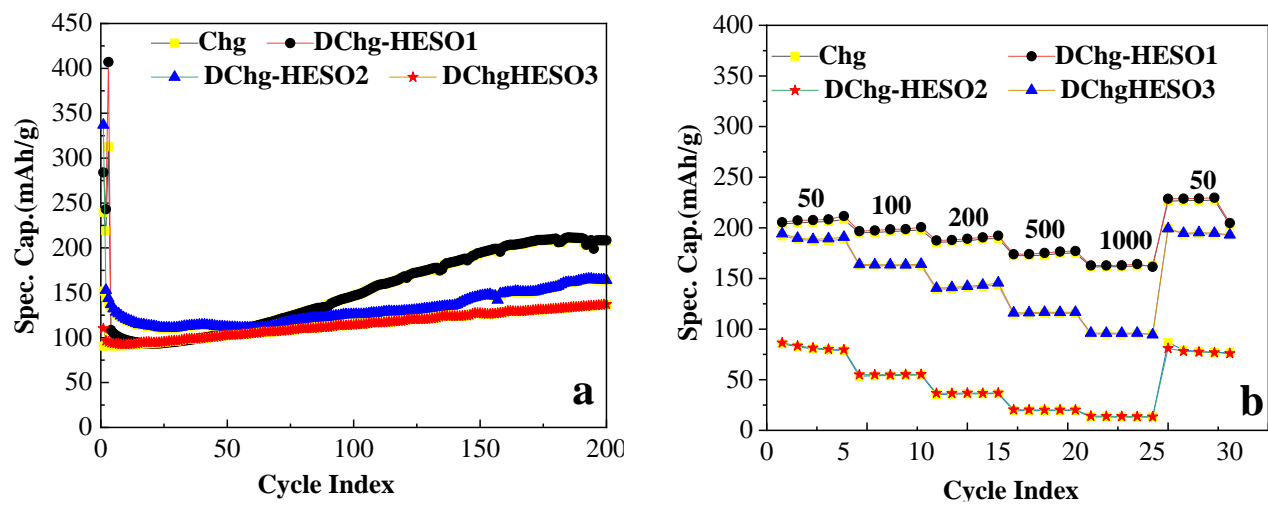
High-entropy oxides with a spinel structure as lithium-ion battery anode materials

Figure 4: (a) cycling performance of HESOs at 200 mAg^{-1} and (b) rate performance of HESOs.

200, 500, and 1000 mAg^{-1} is displayed in Figure 4b. At 1000 mAg^{-1}, the electrodes HESO1, HESO2, and HESO3 have discharge capacities of 163, 14, and 95 mAhg^{-1}, respectively. When the current rate was dropped to 50 mAg^{-1}, the capacities of the three electrodes were not only restored but also increased due to the activation of active materials.

Figure 5 shows the Nyquist plots of all HESO anodes after three formation cycles and the equivalent circuit describing these spectra. Each Nyquist plot consists of two semicircles. In the Nyquist diagram, the resistance of R_s represents the resistance of bulk electrolyte and is the first x-axis intercept value. The High-frequency semicircle represents the SEI film resistance (R_{SEI}), while the semicircle at medium-frequency is related to the charge transfer resistance (R_{ct}) at the electrolyte-electrode interface. The Warburg impedance, which represents the diffusion of Li^+ within the electrode, is responsible for the slope of the curve at low-frequency. [36].

Table 2 gives the parameters of the equivalent circuit for three anodes. The results show that the HESO1 electrode has the smallest value of R_{SEI} and R_{Ct} compared to HESO2 and HESO3, suggesting improved cycling and increased charge transfer during the lithiation/delithiation process at the electrode-electrolyte interface.
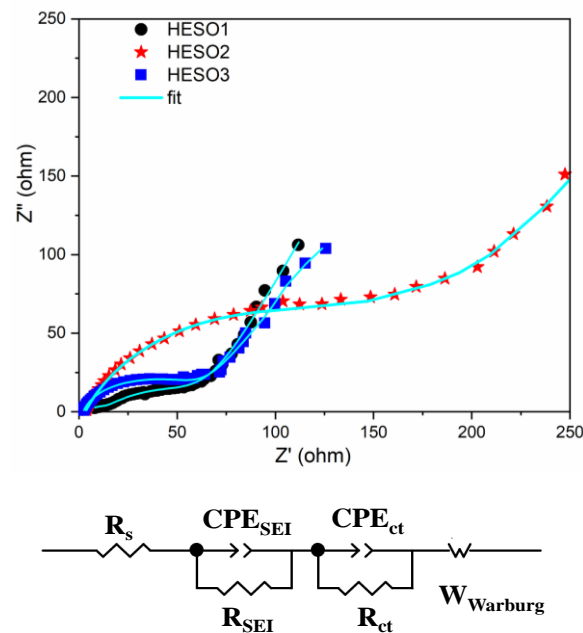

Figure 5: Nyquist plots of HESOs.

Table 2: Parameters of HESO anodes obtained from EIS measurements

Samples	$R_s(\Omega)$	$R_{SEI}(\Omega)$	$R_{ct}(\Omega)$	σ	D_{Li}^+ (cm²/s)
HESO1	2.665	20.15	26.29	10.27	2.22×10^{-13}
HESO2	3.172	27.5	134	57.74	1.61×10^{-13}
HESO3	2.142	20.49	35.39	14.14	0.39×10^{-13}

The Warburg factor (σ) and lithium diffusion coefficient (D_{Li+}) were calculated using equations (2) and (3), respectively [11,37]

$$Z' = R_s + R_{SEI} + R_{ct} + \sigma\,\omega^{-0.5} \qquad (2)$$

$$D_{Li+} = R^2\,T^2\,/\,2A^2\,n^4\,F^4\,C^2\,\sigma^2 \qquad (3)$$

where Z' represents the real part of resistance, A is the electrode's surface area, F is Faraday's constant, T is the absolute temperature, R is the gases constant, ω is the angular frequency, and C is the molar concentration of Li-ion in an active material. Table 2 presents the D_{Li+} values that were determined using the obtained σ. Figure 6 indicates the diagram of the real part resistance versus $\omega^{-0.5}$ at low frequency range for the HESO electrodes. According to Figure 6 and Table 2, D_{Li}^+ for HESO1, HESO2, and HESO3 are $2.22\times10^{-13}, 0.39\times10^{-13}$, and 1.61×10^{-13} cm^2s^{-1}, respectively. It can be seen that HESO1 has a higher D_{Li+} due to its lower σ, which can significantly improve the charging and discharging performance by accelerating the transfer of lithium ions during the electrochemical reaction process [10,11,36].
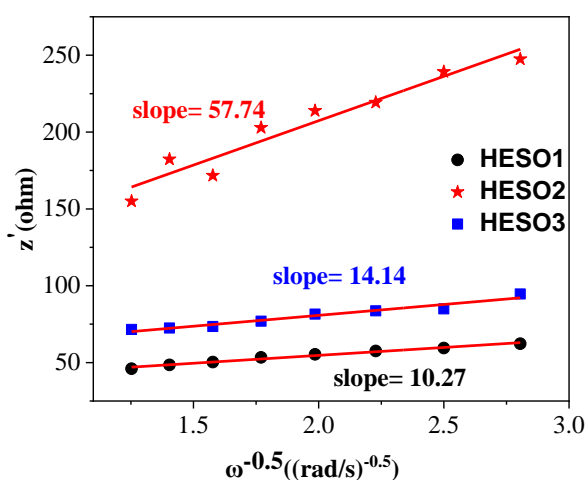

Figure 6: The Z' and $\omega^{-0.5}$ relationship for the three samples at low frequencies.

4. Conclusions

In this study, three single-phase composites $(Mg_{0.6}Ni_{0.6}Ti_{0.6}Fe_{0.6}Zn_{0.6})O_4$, $(Mg_{0.6}Ni_{0.6}Ti_{0.3}Fe_{0.9}Zn_{0.6})O_4$, and $(Mg_{0.6}Ni_{0.6}Ti_{0.3}Zn_{0.9}Fe_{0.6})O_4$ were successfully synthesized through solid state reaction using ball milling.
The effects of increasing and decreasing the content of elements with different lithium storage mechanisms on the properties of the HEOs were investigated.

The conversion and alloying mechanism of li^+ storage are more favorable than the intercalation process in the prepared anodes. In this study, the high entropy oxide composition with a higher content of the element (Ti) with intercalation mechanism, $(Mg_{0.6}Ni_{0.6}Ti_{0.6}Fe_{0.6}Zn_{0.6})O_4$, showed a higher capacity and generally better electrochemical properties than $(Mg_{0.6}Ni_{0.6}Ti_{0.3}Fe_{0.9}Zn_{0.6})O_4$, and $(Mg_{0.6}Ni_{0.6}Ti_{0.3}Fe_{0.6}Zn_{0.9})O_4)$ electrodes. Considering the unpredictable nature of high-entropy oxides, this result was expected.

Declaration of Conflicting Interests

The author(s) declared no potential conflicts of interest with respect to the research, authorship, and/or publication of this article.

Acknowledgments

References

[1] Y. Ma, Y. Ma, Q. Wang, S. Schweidler, M. Botros, T. Fu, H. Hahn, T. Brezesinski, B. Breitung, High-entropy energy materials: challenges and new opportunities, Energy Environ. Sci. 14 (2021) 2883–2905. https://doi.org/10.1039/D1EE00505G.

[2] H.-Z. Xiang, H.-X. Xie, Y.-X. Chen, H. Zhang, A. Mao, C.-H. Zheng, Porous spinel-type (Al0.2CoCrFeMnNi)0.58O4-δ high-entropy oxide as a novel high-performance anode material for lithium-ion batteries, J. Mater. Sci. 56 (2021) 8127–8142. https://doi.org/10.1007/s10853-021-05805-5.

[3] D. Xia, H. Gao, M. Li, F. Gong, M. Li, Transition metal vanadates electrodes in lithium-ion batteries: A holistic review, Energy Storage Mater. 35 (2021) 169–191. https://doi.org/10.1016/j.ensm.2020.10.023 .

[4] M. Sarshar, M. Zarei-Jelyani, M. Babaiee, Application of semi empirical and Multiphysics models in simulating lithium ion battery operation, 10th Int. Chem. Eng. Congr. Exhib. (IChEC 2018) Isfahan, Iran, 6-10 May. (2018). https://www.researchgate.net/profile/Moha mmad-Zarei-

Jelyani/publication/325010205_Applicatio n_of_semi_empirical_and_Multiphysics_ models_in_simulating_lithium_ion_battery _operation/links/5b02ad9ba6fdccf9e4f6ee 6c/Application-of-semi-empirical-and-Multiphysi.

[5] M. Babaiee, S. Baktashian, M. Zarei-Jelyani, R. Eqra, M. Gholami, High-Performance Natural Graphite Anode for Lithium-Ion Batteries: Using TiO_2 as an Additive, ChemistrySelect. 7 (2022). https://doi.org/10.1002/slct.202201510.

[6] A. Barré, B. Deguilhem, S. Grolleau, M. Gérard, F. Suard, D. Riu, A review on lithium-ion battery ageing mechanisms and estimations for automotive applications, J. Power Sources. 241 (2013) 680–689. https://doi.org/10.1016/j.jpowsour.2013.05 .040.

[7] M. Lowe, S. Tokuoka, T. Trigg, G. Gereffi, Lithium-ion batteries for electric vehicles, US Value Chain. Contrib. CGGC Res. Ansam Abayechi. (2010).

[8] X. Yu, B. Qu, Y. Zhao, C. Li, Y. Chen, C. Sun, P. Gao, C. Zhu, Growth of Hollow Transition Metal (Fe, Co, Ni) Oxide Nanoparticles on Graphene Sheets through Kirkendall Effect as Anodes for High-Performance Lithium-Ion Batteries, Chem. – A Eur. J. 22 (2016) 1638–1645. https://doi.org/10.1002/chem.201503897.

[9] X. Li, L. Chen, Y. Qu, Y. Ma, Carbon-assisted conversion reaction-based oxide nanomaterials for lithium-ion batteries, Sustain. Energy Fuels. 2 (2018) 1124–1140. https://doi.org/10.1039/C7SE00620A.

[10] C. Liu, J. Bi, L. Xie, X. Gao, J. Rong, High entropy spinel oxides (CrFeMnNiCox)3O4 (x = 2, 3, 4) nanoparticles as anode material towards electrochemical properties, J. Energy Storage. 71 (2023) 108211. https://doi.org/10.1016/j.est.2023.108211.

[11] H. Xiang, H. Xie, Y. Chen, H. Zhang, A. Mao, C.-H. Zheng, Porous spinel-type (Al0.2CoCrFeMnNi)0.58O4-δ high-entropy oxide as a novel high-performance anode material for lithium-ion batteries, J. Mater. Sci. 56 (2021) 8127–8142.

https://doi.org/10.1007/s10853-021-05805-5.

[12] C. Duan, K. Tian, X. Li, D. Wang, H. Sun, R. Zheng, Z. Wang, Y. Liu, New spinel high-entropy oxides (FeCoNiCrMnXLi)3O4 (X = Cu, Mg, Zn) as the anode material for lithium-ion batteries, Ceram. Int. 47 (2021) 32025–32032. https://doi.org/10.1016/j.ceramint.2021.08. 091.

[13] A. Amiri, R. Shahbazian-Yassar, Recent progress of high-entropy materials for energy storage and conversion, J. Mater. Chem. A. 9 (2021) 782–823. https://doi.org/10.1039/D0TA09578H.

[14] Y. Chen, H. Fu, Y. Huang, L. Huang, X. Zheng, Y. Dai, Y. Huang, W. Luo, Opportunities for High-Entropy Materials in Rechargeable Batteries, ACS Mater. Lett. 3 (2021) 160–170. https://doi.org/10.1021/acsmaterialslett.0c0 0484.

[15] Z. Sun, Y. Zhao, C. Sun, Q. Ni, C. Wang, H. Jin, High entropy spinel-structure oxide for electrochemical application, Chem. Eng. J. 431 (2022) 133448. https://doi.org/10.1016/j.cej.2021.133448.

[16] C.M. Rost, E. Sachet, T. Borman, A. Moballegh, E.C. Dickey, D. Hou, J.L. Jones, S. Curtarolo, J.-P. Maria, Entropy-stabilized oxides, Nat. Commun. 6 (2015) 8485. https://doi.org/10.1038/ncomms9485.

[17] J. Patra, T.X. Nguyen, C. Tsai, O. Clemens, J. Li, P. Pal, W.K. Chan, C. Lee, H.T. Chen, J. Ting, J. Chang, Effects of Elemental Modulation on Phase Purity and Electrochemical Properties of Co-free High-Entropy Spinel Oxide Anodes for Lithium-Ion Batteries, Adv. Funct. Mater. 32 (2022) 1–12. https://doi.org/10.1002/adfm.202110992.

[18] X. Zou, Y. Zhang, Z. Huang, K. Yue, Z. Guo, High-entropy oxides: an emerging anode material for lithium-ion batteries, Chem. Commun. 59 (2023) 13535–13550. https://doi.org/10.1039/D3CC04225A.

[19] M. V. Reddy, G. V. Subba Rao, B.V.R. Chowdari, Metal Oxides and Oxysalts as

Anode Materials for Li Ion Batteries, Chem. Rev. 113 (2013) 5364–5457. https://doi.org/10.1021/cr3001884.

[20] M. Moździerz, K. Świerczek, J. Dąbrowa, M. Gajewska, A. Hanc, Z. Feng, J. Cieślak, M. Kądziołka-Gaweł, J. Płotek, M. Marzec, A. Kulka, High-Entropy Sn 0.8 (Co 0.2 Mg 0.2 Mn 0.2 Ni 0.2 Zn 0.2) 2.2 O 4 Conversion-Alloying Anode Material for Li-Ion Cells: Altered Lithium Storage Mechanism, Activation of Mg, and Origins of the Improved Cycling Stability, ACS Appl. Mater. Interfaces. 14 (2022) 42057–42070. https://doi.org/10.1021/acsami.2c11038.

[21] A. Sarkar, B. Breitung, H. Hahn, High entropy oxides: The role of entropy, enthalpy and synergy, Scr. Mater. 187 (2020) 43–48. https://doi.org/10.1016/j.scriptamat.2020.05.019.

[22] B. Xiao, G. Wu, T. Wang, Z. Wei, Y. Sui, B. Shen, J. Qi, F. Wei, J. Zheng, High-entropy oxides as advanced anode materials for long-life lithium-ion Batteries, Nano Energy. 95 (2022) 106962. https://doi.org/10.1016/j.nanoen.2022.106962.

[23] K.-H. Tian, C.-Q. Duan, Q. Ma, X.-L. Li, Z.-Y. Wang, H.-Y. Sun, S.-H. Luo, D. Wang, Y.-G. Liu, High-entropy chemistry stabilizing spinel oxide (CoNiZnXMnLi)3O4 (X = Fe, Cr) for high-performance anode of Li-ion batteries, Rare Met. 41 (2022) 1265–1275. https://doi.org/10.1007/s12598-021-01872-4.

[24] A. Sarkar, L. Velasco, D. Wang, Q. Wang, G. Talasila, L. de Biasi, C. Kübel, T. Brezesinski, S.S. Bhattacharya, H. Hahn, B. Breitung, High entropy oxides for reversible energy storage, Nat. Commun. 9 (2018) 3400. https://doi.org/10.1038/s41467-018-05774-5.

[25] J. Arshad, N.K. Janjua, R. Raza, Synthesis of Novel (Be,Mg,Ca,Sr,Zn,Ni)3O4 High Entropy Oxide with Characterization of Structural and Functional Properties and Electrochemical Applications, J. Electrochem. Sci. Technol. 12 (2021) 112–125. https://doi.org/10.33961/jecst.2020.01130.

[26] J. Sushil, A. Kumar, A. Gautam, M.I. Ahmad, High entropy phase evolution and fine structure of five component oxide (Mg, Co, Ni, Cu, Zn)O by citrate gel method, Mater. Chem. Phys. 259 (2021) 124014. https://doi.org/10.1016/j.matchemphys.2020.124014.

[27] D. Wang, S. Jiang, C. Duan, J. Mao, Y. Dong, K. Dong, Z. Wang, S. Luo, Y. Liu, X. Qi, Spinel-structured high entropy oxide (FeCoNiCrMn)3O4 as anode towards superior lithium storage performance, J. Alloys Compd. 844 (2020) 156158. https://doi.org/10.1016/j.jallcom.2020.156158.

[28] H. Ji, A. Urban, D.A. Kitchaev, D.-H. Kwon, N. Artrith, C. Ophus, W. Huang, Z. Cai, T. Shi, J.C. Kim, H. Kim, G. Ceder, Hidden structural and chemical order controls lithium transport in cation-disordered oxides for rechargeable batteries, Nat. Commun. 10 (2019) 592. https://doi.org/10.1038/s41467-019-08490-w.

[29] K. Kang, G. Ceder, Factors that affect Li mobility in layered lithium transition metal oxides, Phys. Rev. B. 74 (2006) 094105. https://doi.org/10.1103/PhysRevB.74.094105.

[30] T.-Y. Chen, S.-Y. Wang, C.-H. Kuo, S.-C. Huang, M.-H. Lin, C.-H. Li, H.-Y.T. Chen, C.-C. Wang, Y.-F. Liao, C.-C. Lin, Y.-M. Chang, J.-W. Yeh, S.-J. Lin, T.-Y. Chen, H.-Y. Chen, In operando synchrotron X-ray studies of a novel spinel (Ni 0.2 Co 0.2 Mn 0.2 Fe 0.2 Ti 0.2) 3 O 4 high-entropy oxide for energy storage applications, J. Mater. Chem. A. 8 (2020) 21756–21770. https://doi.org/10.1039/D0TA06455F.

[31] C. Liu, J. Bi, L. Xie, X. Gao, L. Meng, Preparation and electrochemical properties of two novel high entropy spinel oxides (MgTiZnNiFe)3O4 and (CoTiZnNiFe)3O4 by solid state reaction, Mater. Today Commun. 35 (2023) 106315. https://doi.org/10.1016/j.mtcomm.2023.106315.

High-entropy oxides with a spinel structure as lithium-ion battery anode materials

[32] L. Qian, J. Li, G. Lan, Y. Wang, S. Cao, L. Bai, R. Zheng, Z. Wang, S.K. Bhargava, H. Sun, H. Arandiyan, Y. Liu, Towards Low-Voltage and High-Capacity Conversion-Based Oxide Anodes by Configuration Entropy Optimization, ChemElectroChem. 10 (2023) 1–8. https://doi.org/10.1002/celc.202201012.

[33] J. Zhang, G.-H. Lee, V. Wing-hei Lau, F. Zou, Y. Wang, X. Wu, X.-L. Wang, C.-L. Chen, C.-J. Su, Y.-M. Kang, Electrochemical grinding-induced metallic assembly exploiting a facile conversion reaction route of metal oxides toward Li ions, Acta Mater. 211 (2021) 116863. https://doi.org/10.1016/j.actamat.2021.116863.

[34] X. Yang, H. Wang, Y. Song, K. Liu, T. Huang, X. Wang, C. Zhang, J. Li, Low-Temperature Synthesis of a Porous High-Entropy Transition-Metal Oxide as an Anode for High-Performance Lithium-Ion Batteries, ACS Appl. Mater. Interfaces. 14 (2022) 26873–26881. https://doi.org/10.1021/acsami.2c07576.

[35] C. Liu, J. Bi, L. Xie, X. Gao, L. Meng, Electrochemical properties of four novel high-entropy spinel oxides used as lithium-ion battery anodes synthesized by the glycine-nitrate SCS method, J. Mater. Sci. 58 (2023) 8005–8021. https://doi.org/10.1007/s10853-023-08498-0.

[36] M. Zarei-Jelyani, M. Babaiee, S. Baktashian, R. Eqra, Unraveling the role of binder concentration on the electrochemical behavior of mesocarbon microbead anode in lithium–ion batteries: understanding the formation of the solid electrolyte interphase, J. Solid State Electrochem. 23 (2019) 2771–2783. https://doi.org/10.1007/s10008-019-04381-8.

[37] M. Babaiee, S. Baktashian, M. Zarei-Jelyani, R. Eqra, Surface Modification of Copper Current Collector to Improve the Mechanical and Electrochemical Properties of Graphite Anode in Lithium-Ion Battery, J. Renew. Energy Environ. 9 (2022) 63–69. https://doi.org/10.30501/jree.2021.290435.1219).